SUPPLEMENTARY MATERIAL

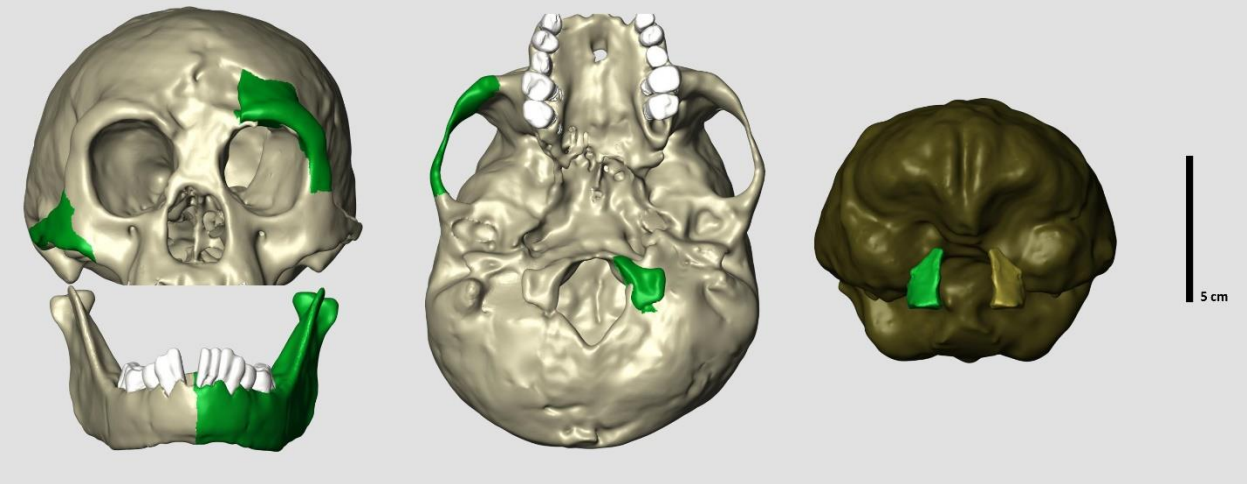

Supplementary Figure 1. Mirror imaging of missing or damaged parts in the LB1 skull from the preserved side, including the right zygomatic arch, left supraorbital, and left mandible.

Supplementary Table 1. List of anatomical landmarks and curves included in the template of KNM-ER 1813.

Unpaired landmarks	**Paired landmarks***	**Curve names**	**#**	**Smln count****
Basion (ba)	Orbitale (or)	Lower zygomatic arc right	1	20
Opistion (o)	Foramen infraorbitale (fori)	Temporal line right	2	19
Stafilion (sta)	Superior orbital notch (son)	Upper zygomatic arc right	3	20
Incisive foramen (if)	Frontotemporale (ft)	Orbital rim right (or to son)	4	9
Glabella (g)	Jugale (ju)	Orbital rim right (son to or)	5	9
Inion (i)	Porion (po)	Anterior nasal aperture left	6	10
Rhinion (rh)	Anterior eminence (ae)	Anterior nasal aperture right	7	10
Anterior nasal spine (ans)	Mastoid process (mp)	Orbital rim left (or to son)	8	9
	Condylus occipitalis posterior (cop)	Orbital rim left (son to or)	9	9
	Entoglenoid (eg)	Temporal line left	10	19
		Upper zygomatic arc left	11	20
		Lower zygomatic arc left	12	20
		Midsagittal	13	39
		Rhinion to glabella (Sellion)	14	9
		Median nucal line	15	9
		Palatine suture	16	9
		Rhinion to Incisive foramen	17	9
		Basisphenoid	18	10
		Internal alveolar rim right	19	10
		Internal alveolar rim left	20	10
		External alveolar rim right	21	10
		External alveolar rim left	22	10
		Total landmarks		**28**
		Total semilandmarks on curves		**299**
		Total semilandmarks on surface		**542**
		Total		869

* Landmarks identifiable on the left and right sides.

** Semilandmarks identified on the curves.

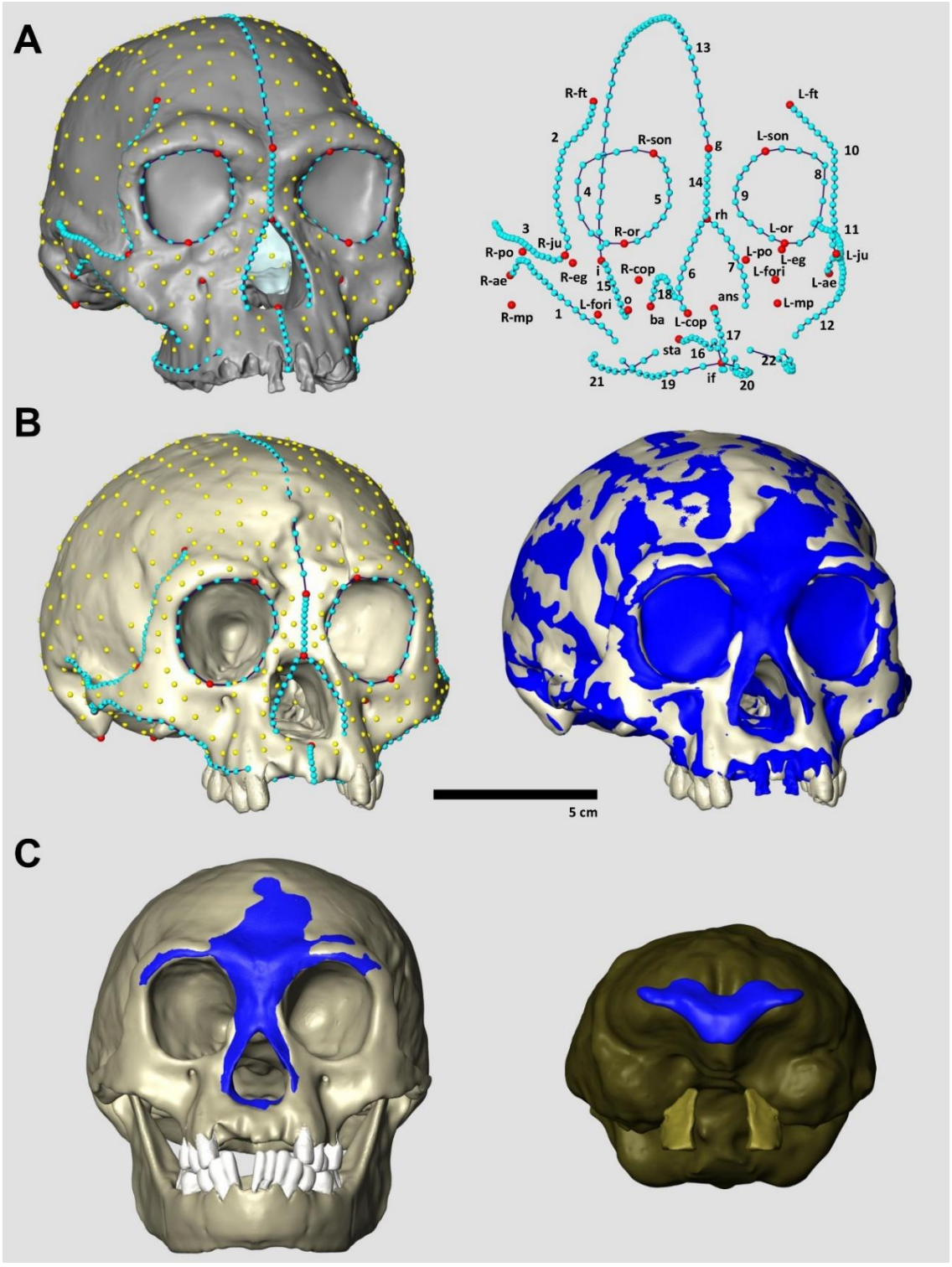

Supplementary Figure 2. Remaining missing portions of LB1 (i.e., bregmatic, nasal, and sub nasal regions) were virtually restored by warping a reference cranium, KNM-ER 1813 (*Homo habilis*), using thin plate spline (TPS) interpolation. (**A**) Reference (semi)landmark configuration (see Supplementary Table 1), (**B**) (semi)landmark configuration applied on LB1 by TPS interpolation (left) and the warping of the KNM-ER 1813 surface on LB1 so as to minimize the bending energy of the according TPS interpolation (right), (**C**) integration of missing parts in the external surface (left) and in the neurocranium (right) of LB1.

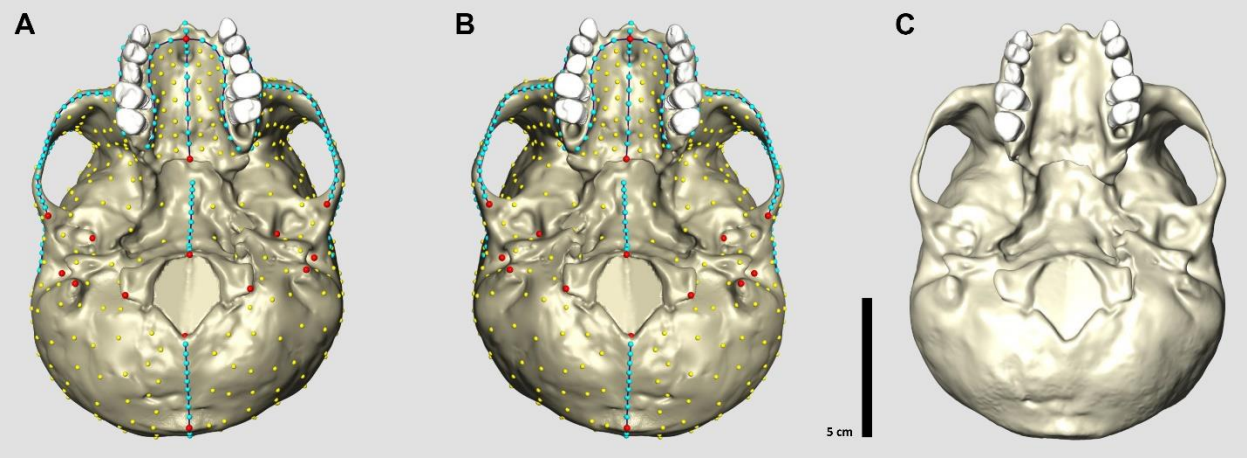

Supplementary Figure 3. The (semi)landmark configuration applied to the reconstructed LB1 cranium (**A**) and its reflected relabeling counterpart (**B**). The average between these two represents the symmetric version of LB1 (**C**).

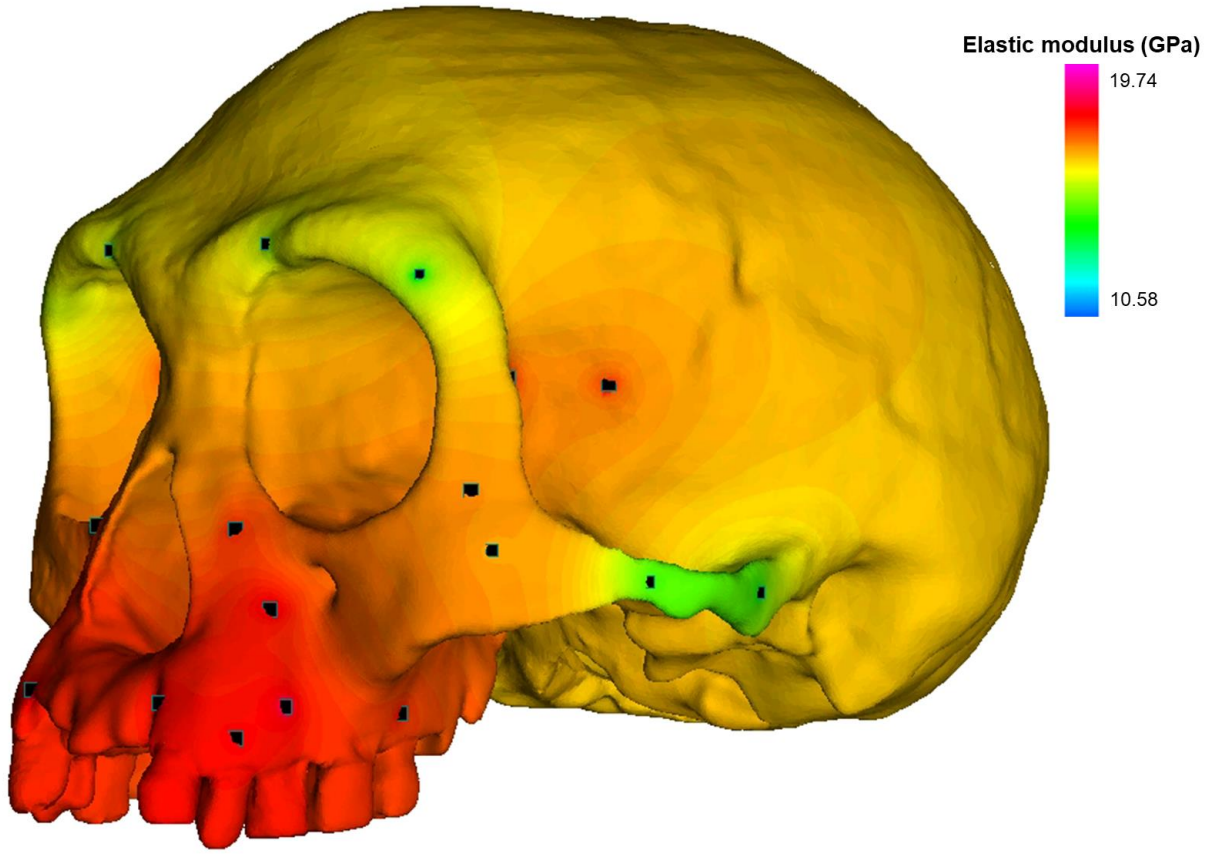

Supplementary Figure 4. Thermal diffusion of elastic modulus (*E*) through the cranium of LB1. "Warm" colours depict regions of high stiffness, while "cool" colours depict regions of lower stiffness. Black squares indicate locations of nodes that were seeded with temperatures corresponding to modulus data collected from one fresh frozen chimpanzee and one fresh frozen gorilla [1–3].

Supplementary Figure 5. The LB1 cranium and mandible in transparent view illustrating locations of plate elements representing the masticatory muscle origins and insertions.

Supplementary Table 2. Scaling of muscle forces applied to finite element models. Muscle forces in Newtons (N) were scaled by model size, where size is represented by model volume in mm^3. Specimen labels for chimpanzees are from Smith et al. [1], while those for modern humans are from Ledogar et al. [4]. Sts 5 = *Australopithecus africanus*, MH1 = *A. sediba*, OH5 = *Paranthropus boisei*, LB1 = *Homo floresiensis*.

Model		Volume (mm^3)	Volume$^{2/3}$	Factor	Muscle Force (N)			
					AT	SM	DM	MPT
Chimpanzees	PC1+	285,969	4,340.60	--	504.00	518.40	77.10	171.30
	PC1-	363,139	5,090.00	0.17	591.19	608.08	90.44	200.93
	PC2+	263,980	4,115.10	-0.05	477.79	491.44	73.09	162.39
	PC2-	285,236	4,333.10	0.00	503.14	517.52	76.97	171.01
	PC3+	394,911	5,382.69	0.24	623.90	641.72	95.44	212.05
	PC3-	418,252	5,592.75	0.29	648.25	666.77	99.17	220.33
Humans	GRGL	557,223	6,771.52	1.56	786.26	808.73	120.28	267.24
	BERG	489,588	6,211.84	1.43	721.28	741.88	110.34	245.15
	KSAN1	433,331	5,726.38	1.32	664.91	683.90	101.71	225.99
	KSAN2	331,466	4,789.53	1.10	556.13	572.02	85.07	189.02
	MALP	364,129	5,099.22	1.17	592.09	609.00	90.57	201.24
	TIGA	655,320	7,544.59	1.74	876.02	901.05	134.01	297.74
	WAFR	475,555	6,092.57	1.40	707.43	727.64	108.22	240.44
Fossils	Sts 5	347,264	4,940.53	1.14	573.66	590.05	87.76	194.98
	MH1	305,801	4,538.99	1.05	527.04	542.09	80.62	179.13
	OH5	708,959	7,950.86	1.83	923.20	949.57	141.23	313.78
	LB1	286,223	4,343.13	1.00	504.29	518.70	77.14	171.40

Supplementary Table 3. The von Mises microstrain (με) magnitudes sampled from 14 craniofacial sites during simulations of P^3 and M^2 biting in FEMs of modern chimpanzees [1], modern humans [4], *Homo floresiensis* (LB1; this study), *Australopithecus sediba* (MH1; [5]), *Paranthropus boisei* (OH5; [6]), and *A. africanus* (Sts 5; [6]). See Figure 4 (Main Text) for key to craniofacial locations.

Location	Bite	Chimpanzee Range	Human Range	LB1	MH1	OH5	Sts5
DIT	P^3	160 – 271	213 – 438	134	106	214	243
	M^2	145 – 250	172 – 309	129	102	170	222
WDO	P^3	32 – 189	227 – 397	145	98	70	189
	M^2	26 – 120	145 – 266	123	80	72	191
BDO	P^3	146 – 268	248 – 445	158	124	138	136
	M^2	150 – 284	258 – 423	167	139	203	136
WPB	P^3	276 – 810	1,226 – 1,762	1,155	431	238	872
	M^2	216 – 692	542 – 1,137	960	356	228	640
BPB	P^3	504 – 1,115	1,405 – 2,092	1,272	527	461	1,217
	M^2	492 – 1,175	1,428 – 2,011	1,327	556	555	1,234
WZA	P^3	757 – 4,791	990 – 1,563	2,069	445	431	1,784
	M^2	662 – 4,832	875 – 1,394	2,096	392	733	1,776
BZA	P^3	686 – 3,549	1,147 – 1,503	2,064	622	509	3,164
	M^2	666 – 3,542	1,116 – 1,462	2,077	595	509	3,171
WZR	P^3	788 – 1,202	1,443 – 1,932	1,316	712	624	1,300
	M^2	795 – 1,803	1,870 – 2,773	1,440	971	466	2,188
BZR	P^3	350 – 644	483 – 689	565	330	244	520
	M^2	375 – 747	576 – 729	602	346	274	576
WIF	P^3	560 – 916	858 – 1,136	1,057	608	536	636
	M^2	632 – 935	819 – 1,170	823	485	282	504
BIF	P^3	304 – 722	561 – 756	696	360	468	635
	M^2	287 – 660	435 – 665	563	326	345	574
WNM	P^3	625 – 1,183	1,363 – 3,900	4,773	803	547	1,600
	M^2	211 – 625	534 – 1,543	1,221	125	313	352
WZB	P^3	793 – 1,424	283 – 635	1,044	564	382	632
	M^2	847 – 1,497	655 – 975	1,153	548	394	638
BZB	P^3	502 – 2,048	261 – 502	809	430	347	783
	M^2	477 – 1,996	267 – 525	781	399	322	775

REFERENCES

1. Smith AL, Benazzi S, Ledogar JA, Tamvada K, Smith LCP, Weber GW, Spencer MA, Dechow PC, Grosse IR, Ross CF, et al. Biomechanical implications of intraspecific shape variation in chimpanzee crania: moving toward an integration of geometric morphometrics and finite element analysis. 2015;144:122–44.
2. Schwartz-Dabney CL, Dechow PC. Accuracy of elastic property measurement in mandibular cortical bone is improved by using cylindrical specimens. J Biomech Eng. 2002;124(6):714–23.

3. Schwartz-Dabney CL, Dechow PC. Variations in cortical material properties throughout the human dentate mandible. Am J Phys Anthropol. 2003;120(3):252–77.
4. Ledogar JA, Dechow PC, Wang Q, Poorva H, Gordon AD, Baab KL, Smith AL, Weber GW, Grosse IR, Ross CF, et al. Human feeding biomechanics: performance, variation, and functional constraints. PeerJ. 2016;(1):1–47.
5. Ledogar JA, Smith AL, Benazzi S, Weber GW, Spencer MA, Carlson KB, McNulty KP, Dechow PC, Grosse IR, Ross CF, et al. Mechanical evidence that *Australopithecus sediba* was limited in its ability to eat hard foods. Nat Commun. 2016;7:10596.
6. Smith AL, Benazzi S, Ledogar JA, Tamvada K, Pryor Smith LC, Weber GW, Spencer MA, Lucas PW, Michael S, Shekeban A, et al. The feeding biomechanics and dietary ecology of *Paranthropus boisei*. Anat Rec. 2015;298(1):145–67.